Monolithic, 3D-Printed Microfluidic Platform for Recapitulation of Dynamic Tumor Microenvironments

Ashley L. Beckwith, Jeffrey T. Borenstein, and Luis Fernando Velásquez-García, *Senior Member, IEEE*

***Abstract*— We report the development of an entirely 3D-printed, monolithic microfluidic platform that provides a dynamic microenvironment for perfusing and sustaining tumor fragments from a biopsy sample. The finely featured, non-cytotoxic, and transparent tumor trap is integrated with threaded connectors for rapid, leak-proof fluid interfacing, an in-line trap for removal of bubbles arising from oxygenated media flow or tumor loading procedures, and a network of microchannels for supplying media (and potentially immune cells) to the trapped tumor fragment. The devices were additively manufactured in Pro3dure GR-10 –a relatively new, high-resolution stereolithographic resin with properties suitable for biomedical applications requiring interrogation via fluorescence microscopy. Overlaid bright-field and fluorescence microscopy images demonstrate trapping of human tumor fragments by the printed microfluidic device, as well as visualization of individual cells within the fragment. A multi-day trapping experiment evidences the ability to sustain a live tumor fragment under dynamic perfusion within the device–a configuration capable of modeling of interactions between tumors and various drug treatments in the presence of circulating immune cells, e.g., for assessment of the efficacy of chemotherapy and immunotherapy treatments. [2018-0048]**

***Index Terms*— 3D printed MEMS, bioMEMS, cytotoxicity, microfluidics, stereolithography, tumor trap.**

I. Introduction

MICROFLUIDICS enable precise manipulation of small volumes of fluid for the investigation and analysis of microscopic physical, chemical, and biological phenomena. Device miniaturization and batch fabrication have traditionally translated into reductions in cost, materials, and time required for experimental execution [1]. These attributes render microfluidic devices promising platforms for clinical investigations, which demand judicious and economical analysis methods –as procurement of biological samples often comes at the expense of a patient's physical and financial well-being.

Manuscript received March 4, 2018; revised August 2, 2018; accepted September 1, 2018. Date of publication October 15, 2018; date of current version November 29, 2018. This work was supported in part by the Draper Fellowship Program through The Charles Stark Draper Laboratory, Inc., Cambridge, MA, USA. Subject Editor D. DeVoe. *(Corresponding author: Luis Fernando Velásquez-García.)*

A. L. Beckwith is with the Department of Mechanical Engineering, Massachusetts Institute of Technology, Cambridge, MA 02139 USA (e-mail: ashbeck@mit.edu).

J. T. Borenstein is with The Charles Stark Draper Laboratory, Inc., Cambridge, MA 02141 USA (e-mail: jborenstein@draper.com).

L. F. Velásquez-García is with the Microsystems Technology Laboratories, Massachusetts Institute of Technology, Cambridge, MA 02139 USA (e-mail: velasquez@alum.mit.edu).

Color versions of one or more of the figures in this paper are available online at http://ieeexplore.ieee.org.

Digital Object Identifier 10.1109/JMEMS.2018.2869327

Microfluidic devices for the laboratory-based investigation of drug effects on tumor growth, development, and metastasis are rapidly emerging [2]–[11]. More accurate *in vitro* models of the tumor microenvironment would provide better platforms for investigating the effectiveness of chemotherapy and immunotherapy agents in early stages of pharmaceutical development, reducing the cost and risk involved in preclinical studies. Improved, clinically-relevant models could also provide benefits in guiding treatment administration.

Despite the increasing prevalence of sophisticated microfluidic cell-culture models developed for research applications [6]–[11], microfluidic technology remains underutilized in the clinical setting. A particular application that may benefit from the implementation of microfluidic models is the prediction of patient response to chemotherapeutics and immunotherapeutics. Unfortunately, existing cell-culture models are not generally equipped to support timely and facile analyses. Microfluidic devices intended to provide insight into tumor microenvironments are often designed to evaluate cell-culture systems or engineered tumor spheroids [2]–[4], [12], [13]. In this work, we utilize fragments of tumor biopsies as a basis for investigation. While tumor spheroids can take weeks to grow [3] (and may be difficult to obtain for some cancer types [2]), evaluation of tumor fragments resected from patients can begin within 24 hours of patient biopsy. The implementation of intact native tissue addresses two key concerns with tumor spheroid models, i.e., inability to ensure development of spheroids with density and extracellular matrix composition faithful to *in vivo* conditions [2], and failure of cultured spheroids to reflect the heterogeneity of autochthonous tumor tissue [14].

Ayusa *et al.* [2] underline the importance of implementing three-dimensional tumor models over traditional two-dimensional assays to more accurately evaluate tumor behavior and recapitulate the physiologic microenvironment; this challenge in expanded dimensionality, evident throughout the field of microscale physiological modelling, demands microfluidic devices of increasing complexity. As microfluidics become more sophisticated, challenges associated with their fabrication and general device usability must be addressed. The preponderance of microfluidic devices is fabricated with soft lithography, i.e., a technique that creates predominantly planar structures via micromolding of polydimethylsiloxane (PDMS) against a high-resolution master [15]; in particular, many microfluidic devices developed for tumor microenvironment investigations are fabricated in PDMS [3]–[4]. While bio-inert, PDMS is not an ideal material

for many applications due to its natural hydrophobicity and tendency to adsorb or absorb proteins and small-molecule drugs–a trait that can adversely impact the ability to control the concentration of soluble factors in experimental studies [16]. Alternative fabrication methods and materials, such as injection-molded polystyrene [2] or micro-machined glass and plastics [17], have recently been reported. While PDMS alternatives may remedy potential issues with drug adsorption, other problems with traditionally-fabricated microfluidics persist. In addition, standard microfluidic fabrication techniques are often unable to produce certain geometries or features that facilitate device operation, e.g., standardized fluidic ports or effective approaches for bubble removal; failure to adequately consider device integration issues limits the translation of microfluidics from the research laboratory to practical clinical or industrial implementation.

Complex (e.g., three-dimensional) microfluidics are typically manufactured via multi-wafer stacks with substrates made of a plurality of materials that are individually patterned before alignment and bonding [18], [19]; unfortunately, the construction of these devices is laborious, complex, and costly. Consequently, technically challenging assembly processes commonly result in low fabrication yield; material and structural limitations of the mainstream microfabrication processes impose additional design constraints. Furthermore, efforts to leverage traditional microfabrication technologies to implement three-dimensional structures of relevance to MEMS have yielded moderate success [20]–[23].

Additive manufacturing (AM), i.e., the layer-by-layer creation of solid objects, using as a template, a computer-aided design (CAD) file [24], is a promising approach for implementing microfluidic systems [25]–[27]. Accessibility of printing technologies and availability of printable materials that exhibit diverse mechanical, chemical, and optical properties make AM practical for many applications and user-experience levels. In addition to greater flexibility in the types of component geometries that can be created, AM simplifies the overall development of microfluidic devices and increases process yields, enabling wider acceptance of the devices in research and clinical settings. Moreover, the potential for monolithic construction of a 3D-printed (3DP) microfluidic device via AM eliminates the need for subsequent adhesion or bonding processes, improving the consistency of its manufacturing by eliminating the need for alignment and by limiting operator involvement and potential error in the fabrication. The true 3D capabilities of AM also permit curved fluidic transitions and minimized dead volumes relative to conventional planar fabrication techniques and fluidic port interfacing. In addition, 3D-printing enables rapid and inexpensive iteration of prototypes, serving as an invaluable research tool for the development of novel microfluidic devices. Researchers have reported microfluidics on par or superior to counterparts made with standard microfabrication techniques [28]–[30], demonstrating as well complex devices that are unfeasible or difficult to implement by other means of manufacturing [31], [32].

This study reports a monolithic, fully 3DP Tumor Analysis Platform (TAP) that retains and sustains human tumor tissues *ex vivo* for an extended period of time through the entrainment of tissue fragments under continuous perfusion of media. The proposed TAP device features threaded fluidic connectors that enable rapid and leak-proof fluid interfacing, an in-line trap for evacuation of bubbles introduced during tumor loading or device operation, and a network of microfluidic channels that supply media (and potentially circulating immune cells) to the hosted tumor fragment. Section II explains the considerations made for selecting the printable material with associated printing method including feature resolution, cellular compatibility, transparency, and non-fluorescence. Section III describes the design of the devices, while Section IV describes their fabrication. Section V reports the experimental results, while Section VI summarizes the work and proposes directions for future research.

II. Selection and Characterization of Printable Material with Associated AM Method

Before developing the TAP device, we surveyed the literature on commercial printable materials and talked to vendors, in an effort to identify the best possible choice for the intended application. In this work, the requirements of the printable material include (1) water tightness, (2) non-cytotoxicity over an extended period of time, (3) optical transparency, (4) little to no auto-fluorescence to enable data capture of the device operation via fluorescence images, and (5) high-resolution fabrication to be able to reproduce small features. In general, each printable material is processed via a specific printing method, resulting in distinct limitations. For example, the chemical composition of a certain printable material could facilitate defining very small features using light, but the pigments that give the resin its high resolution also make the printed part opaque. Furthermore, a printing process could fill-in internal voids with photopolymerized support material (e.g., PolyJet printing [33]), which is far harder to remove than uncured material in order to have working microchannels. In addition, a printing process could be inherently too coarse to produce optically clear surfaces (e.g., fused filament fabrication [34]) or use as feedstock powders that create non-leak-tight parts with surfaces that adsorb/absorb species (e.g., selective laser sintering [35]).

From this survey, four materials were down-selected for experimental investigation–all of them are liquid resins with an associated printing process that harnesses photopolymerization to create solid objects. The printable materials tested included *PlasCLEAR* (Asiga, Sydney, Australia)–printed via Digital Light Projection Stereolithography (DLP-SLA), *Watershed XC11122* (DSM Functional Materials, Somos® Material Group, Elgin IL, USA)–printed via stereolithography (SLA), *Pro3dure GR-10* (Pro3dure Medical GmbH, Dortmund, Germany)–printed via DLP-SLA, and MED 610 (Stratasys, Eden Prairie MN, USA)–printed via PolyJet. The DLP-SLA prints were made with a Pico Plus 27 (Asiga, Sydney, Australia), the SLA prints were made with a Viper (3D Systems, Valencia CA, USA), and the PolyJet prints were made with a Objet1000 Plus® printer (Stratasys, Eden Prairie MN, USA). From this exploration, the DLP-SLA printable resin

TABLE I

PRINTING TECHNOLOGY, LEAST-SQUARES LINEAR FIT OF PRINTED PILLAR DIAMETER AS A FUNCTION OF CAD PILLAR DIAMETER, MINIMUM PRINTED DIAMETER, AND LEAST-SQUARES LINEAR FIT OF PRINTED PILLAR HEIGHT AS A FUNCTION OF CAD PILLAR HEIGHT FOR THE SET OF DOWN-SELECTED PRINTABLE MATERIALS

Material	Printing Technology	Linear Fit PD vs. CD (μm)	Smallest PD (μm)	Linear Fit PH vs. CH (μm)
PlasCLEAR	DLP-SLA	$PD = 1.20 \cdot CD - 198, R^2 = 0.97$	90.5 ± 14.5 (16%)	$PH = 0.983 \cdot CH - 66.0, R^2 = 0.84$
WaterShed XC11122	SLA	$PD = 0.978 \cdot CD + 3.39, R^2 = 0.99$	92.2 ± 7.8 (8.5%)	$PH = 0.934 \cdot CH + 0.239, R^2 = 0.99$
Pro3dure GR-10	DLP-SLA	$PD = 1.04 \cdot CD - 40.9, R^2 = 0.99$	134.4 ± 6.3 (4.7%)	$PH = 0.899 \cdot CH + 59.6, R^2 = 0.98$
MED610	PolyJet	$PD = 0.990 \cdot CD + 53.4, R^2 = 0.99$	307.7 ± 10.9 (3.5%)	$PH = 0.881 \cdot CH + 53.4, R^2 = 0.94$

In the linear fits PD = printed pillar diameter, CD = CAD pillar diameter, PH = printed pillar height, and CH = CAD pillar height. Each nominal height value was used in 16 different pillars of each resolution matrix, while each nominal diameter value was used in 8 different pillars of each resolution matrix.

Pro3dure GR-10 was selected as the constitutive material for the TAP devices. Pro3dure GR-10 is a methacrylate-based resin that is intended for manufacturing implant and bite splints [37]. To the best of our knowledge, the resin Pro3dure GR-10 has not been thoroughly characterized in the open literature, particularly in the context of microfluidic development.

A. Convex Feature Resolution Characterization

High-resolution fabrication is essential for the successful implementation of finely featured microfluidics. The printing resolution of each material tested was characterized using a resolution matrix, i.e., an array of features that systematically covers a range of one or more parameters of the morphology of the feature (subsets of features within a resolution matrix, with one or more nominally identical parameters, are intended to characterize the repeatability of the fabrication method). In these experiments, each resolution matrix consisted of an array of straight cylindrical pillars spanning specified ranges of diameter and height. For highest fidelity between prints and CAD files, the nominal diameters of the cylindrical pillars (i.e., in the CAD files) were multiples of the pixelation/spot size of the printing method; the DLP-SLA printer had 30.3 μm pixels, the PolyJet printer had 43.2 μm pixels (both pixel sizes were estimated from preliminary printing experiments), and the SLA printer had a 127 μm laser spot size (from the printer documentation). For the DLP-SLA and PolyJet prints, the nominal diameters were equal to 6, 7, 8, 9, 10, 12, 15, and 20 pixels; even though commercial DLP-SLA printers are capable of printing features with as little as 3 pixels ($\sim$75 μm) [38], such small features are obtained with high-resolution, opaque resins that are incompatible with our application. For the SLA prints, the nominal diameters were equal to 1, 2, 3, 4, 5, 6, 7, and 8 laser spot sizes. Similarly, in all cases the nominal heights of the pillars were multiples of the slicing height (25 μm for all printers) and equal to 250 μm, 500 μm, 750 μm, and 1000 μm.

The resolution matrices were measured with a scanning white light interferometer VR-3100 3-D Measurement System (Keyence, Itasca IL, USA) using the VR-3000 series software. Characterization of each resin tested included evaluation of the similarity between printed and CAD dimensions, assessment of the linearity of the dimensional scaling, and estimation of the minimum in-plane feature size; the summary of the metrology of the different printable materials characterized is shown in Table I. The metrology data show Pro3dure GR-10 and WaterShed XC11122 as the best-performing resins of the set: for example, using the DLP-SLA material PlasCLEAR results in diameters 20% larger than the ideal 1-to-1 correspondence with CAD values–a fivefold larger offset compared to the other resins; also, the smallest diameter resolved by the PolyJet material MED610 is about a threefold larger than the minimum features made via SLA or DLP-SLA, which suggests potential challenges when attempting to create designs with fine features using such material. For Watershed XC11122 (i) there is linearity between the nominal and printed diameters across the examined range with a slope 2% off the ideal 1-to-1 correspondence; (ii) on average, there is very little offset between the diameter of the printed part and the CAD model ($\sim$3.5 μm); (iii) the narrowest printed pillars had a nominal diameter equal to 127 μm, corresponding to a printed diameter equal to 92.2 $\pm$ 7.8 μm; and (iv) the relationship between the printed height and the nominal height of the pillars is also linear, with a slope 7% off from the ideal 1-to-1 correspondence and a sub-micrometer offset. For Pro3dure GR-10 (i) the nominal and printed diameters are linear across the range investigated, with a slope 4% off the ideal 1-to-1 correspondence; (ii) there is an average offset on the order of one pixel between the printed diameter and the diameter of the CAD model; (iii) the narrowest printed pillar had a nominal diameter equal to 181.5 μm, corresponding to a printed diameter equal to 134.4 $\pm$ 6.3 μm; and (iv) the printed height vs. nominal height characteristic of the pillars is also linear, with a slope 10% off the ideal 1-to-1 correspondence and an offset on the order of two slices (60 μm). Even though the smallest diameter resolved with the material Pro3dure GR-10 is $\sim$50% larger than the smallest diameters resolved with the materials PlasCLEAR and Watershed XC11122, the variation of the Pro3dure GR-10 features is smaller in both absolute and relative terms, which should translate into more repeatable fabrication. For Pro3dure GR-10 and WaterShed XC11122, variation in aspect ratio of the pillar features had a minor effect on the accuracy of their heights.

B. Cellular Compatibility

Cytotoxicity testing was performed on the four printable materials down-selected for the TAP device. Long-term viability of cells in contact with the material is required for the intended tumor analysis application because extended exposure of cellular material to the printed material is expected.

However, the literature suggests that many purportedly printable biocompatible materials exhibit varied degrees of cytotoxicity in vitro [39],[40]; furthermore, most photopolymerizable materials that are reportedly biocompatible exhibit obvious cytotoxic effects by the 48-hour mark [40],[41]. In the first round of experiments, viability of cells was monitored during 48-hour exposure to each of the evaluated materials. Based on the experimental results, Pro3dure GR-10, i.e., the material of the set that performed most similarly to the positive control, was selected for an extended 96-hour cytotoxicity test, which confirmed the remarkable cellular compatibility of the resin.

The samples used in these experiments were 6 mm by 6 mm by 2 mm printed tiles. Cleaned samples were placed in a 24-well Falcon well-plate (Corning, Inc., Corning NY, USA). Jurkat immortalized human T-lymphocytes (grown in Roswell Park Memorial Institute with 10% fetal bovine serum, i.e., FBS, and 1:100 penicillin/streptomycin medium) were seeded into wells containing sample tiles (n = 3 samples in total for each resin, 1 per well), or, in the case of the positive control (cells grown on tissue culture polystyrene, i.e., TCPS), no tile (n = 3 wells in total) at a density of 250,000 cells/mL, 1 mL per well. The samples were incubated at a temperature of 37 °C for 48 hours. Using the PrestoBlue® cell viability reagent, cell viability was assessed at three points in time, i.e., immediately after seeding, at 24 hours of incubation, and at 48 hours of incubation. Wells of cell media, without cells, and reagent were incorporated into the assay to act as blanks. Assay wells were mixed thoroughly, and the cells and reagent incubated for one hour at a temperature of 37 °C. A SpectraMax M2 microplate reader (Molecular Devices, Sunnyvale CA, USA) measured the fluorescence levels of the assay wells at an excitation of 560 nm and an emission of 590 nm. Fluorescence values for the media-only treatment group were averaged and subtracted from the fluorescence readings obtained from the remaining treatment groups (i.e., the four resins and the positive control). The blank-corrected values were then averaged across each treatment group. The reported values were normalized to the blank-corrected TCPS average for the respective day; the results are shown in Fig. 1. Two-tailed Student's t-tests performed between each material group and the normalized control value of unity permitted evaluation of statistically significant differences between the test groups and the positive control treatment group. At 48 hours, only Pro3dure GR-10-exposed cells exhibited no statistically significant decline in viability compared to the TCPS control ($\alpha = 0.1$).

The majority of materials tested induced some degree of decline in cell viability over the duration of the test. The MED610, Watershed XC11122, and PlasCLEAR materials demonstrated varied degrees of decline in cell viability over the 48-hour test period. Zhu *et al.* demonstrated similar toxic effects of the Watershed XC11122 material when zebrafish embryos exposed to the material were shown to exhibit developmental abnormalities [39]. However, cells exposed to Pro3dure GR-10 exhibited no decline in cell viability relative to the positive control. The extended viability study for Pro3dure GR-10 reaffirmed the findings of the short-term cytotoxicity study (Fig. 2). The viability of Jurkat human

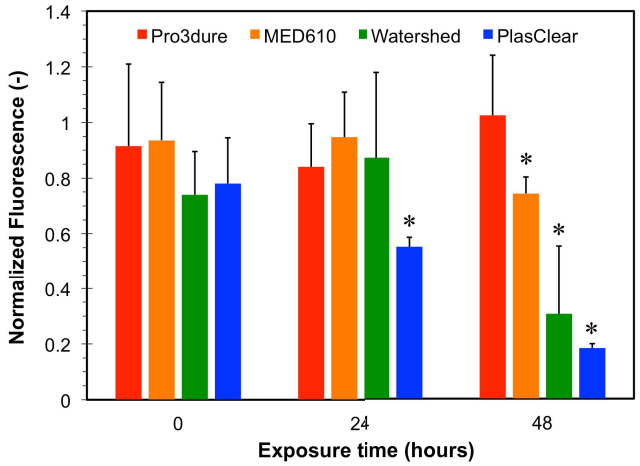

Fig. 1. Cell viability (fluorescence) vs. duration of cellular exposure to printed samples; the fluorescence measurements were normalized to the positive control for the respective day. Error bars represent one standard deviation. Except for Pro3dure GR-10, exposure to all printable materials tested resulted in a statistically significant change in cell viability within 48 hours of exposure ($\alpha = 0.1$). In the figure, a statistically significant difference in cell viability compared to the control is denoted by an asterisk.

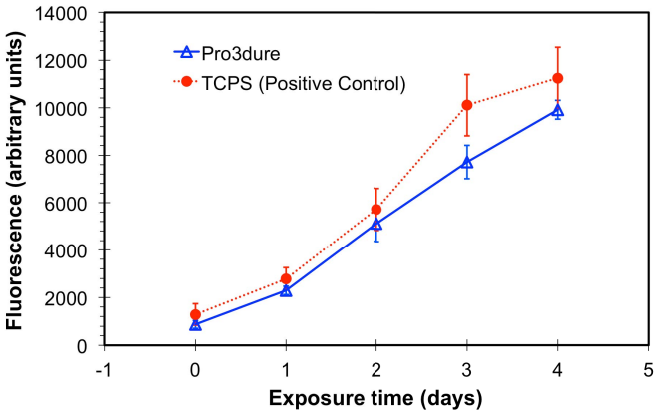

Fig. 2. Cell viability (fluorescence) vs. exposure time to Pro3dure GR-10 pucks. Error bars represent one standard deviation from the average.

T-lymphocytes exposed to Pro3dure GR-10 was not statistically significantly different than the positive control of cells grown in TCPS after 96 hours of exposure to the material. A two-tailed Student's t-test with unequal variance performed at a confidence-level of $\alpha = 0.05$ could not reject the null hypothesis that the two groups had equal means (P = 0.08 for Day 4).

The conclusion of the cytotoxicity and convex feature resolution experiments is that Pro3dure GR-10 is the best material of the examined set for creating microfluidic devices intended for biomedical applications. For example, although WaterShed XC11122 can resolve finer features than Pro3dure GR-10 and printed parts made in this resin have closer resemblance to the CAD file, WaterShed XC11122 exhibits cytotoxicity. Also, even though MED610 has comparable biocompatibility to that of Pro3dure GR-10, its feature resolution is not nearly as good; moreover, MED610 is printed via PolyJet, i.e., it creates channels filled-in with solidified support material, which significantly complicates the post-processing (channel unclogging) of a complex microfluidic device [29]. Therefore, the remaining characterization of the printable feedstock

(i.e., channel resolution, transparency, and fluorescence) focused on the Pro3dure GR-10 resin.

C. Microchannel Resolution Characterization

Understanding the limitations of fabrication technology is integral to the effective design and construction of 3DP microfluidics. Microscale channels and voids, rather than microscale extrusions, are perhaps the more critical attributes of microfluidic devices. Channel fabrication capabilities widely vary depending on the 3D printing method and material; the smallest dimensions of resolvable channels ultimately govern the design of the microfluidic device. Therefore, a full factorial design of experiments (DOE) was conducted for Pro3dure GR-10 to investigate how printing parameters affect the dimensions of microfluidic channels, as well as how these dimensions compare to those of the input CAD file, with the goal of understanding fabrication limitations.

The Asiga Pico Plus 27 used to print Pro3dure GR-10 in this work is a DLP-SLA system in which the build platform is drawn upward from a vat of resin as the part is fabricated layer by layer. The extent of curing in a build is governed in part by the intensity of the printer's UV light source, the duration of UV exposure, and the absorbance characteristics of the photopolymer resin. The creation of microchannels requires precise control of the curing process because over-exposure of the resin to UV light can result in unwanted constriction of channels and voids. In this work, over-curing is defined as the curing of resin beyond the CAD dimensions due to the bleeding of light into the adjacent resin. Minor over-curing is critical to achieve adhesion between printed layers; however, substantial over-curing can lead to prints that unpredictably stray from the CAD model. Two adjustable parameters of the 3D printing job (i.e., the list of parameters that specify the printing process) significantly affect the extent of curing within a build, i.e., *layer thickness* and *curing thickness offset*. The layer thickness is defined as the incremental distance the platform moves vertically with each layer of the build; as each layer is cured, the thickness of the polymerized layer extends beyond the assigned layer thickness and partially into the already solidified material to ensure that the new layer and previous layers are firmly bonded to one another. The curing offset is the distance that this polymerized layer theoretically extends beyond the assigned layer thickness. The curing offset can be directly adjusted within the printer software; alterations to this dimension translate into modified exposure times.

Layer thickness and curing thickness offset were incorporated into a DOE to investigate their combined effects on over-curing within a build. Curing offset levels were selected based on a suggested range provided by the printer manufacturer (i.e., 60 μm, 80 μm, and 100 μm). Test layer thicknesses were restricted to available printer settings within a practical resolution range for desired microfluidic features (i.e., 50 μm, 100 μm, and 150 μm). Over-curing in the build direction (i.e., out of plane) was found to be significantly dependent upon the layer offset and curing thickness ($P < 0.05$). The extent of over-curing tended to decrease with increasing layer thickness and decreasing curing offset. Based on the trends observed, a 100 μm layer thickness and 40 μm curing offset were selected for microfluidic fabrication and found to produce repeatable prints with good adhesion between layers and manageable over-curing; larger layer thicknesses led to reduced over-curing, but increased likelihood of build failure.

TABLE II

CROSS-SECTIONAL AREA FOR A RANGE OF CAD CHANNEL WIDTHS AND HEIGHTS PRINTED WITH PRO3DURE GR-10

Assigned channel cross-sectional area (mm^2)								
		CAD channel width (mm)						
		1.50	1.25	1.00	0.75	0.60	0.50	0.40
CAD channel height (mm)	2.25	3.38	2.81	2.25	1.69	1.35	1.13	0.90
	2.00	3.00	2.50	2.00	1.50	1.20	1.00	0.80
	1.75	2.63	2.19	1.75	1.31	1.05	0.88	0.70
	1.50	2.25	1.88	1.50	1.13	0.90	0.75	0.60
	1.00	1.50	1.25	1.00	0.75	0.60	0.50	0.40
	0.75	1.13	0.94	0.75	0.56	0.45	0.38	0.30
	0.50	0.75	0.63	0.50	0.38	0.30	0.25	0.20

Successfully cleared channels are shaded, while channels that did not successfully resolve (i.e., clogged) are unshaded

Analysis of variance of the DOE data indicated that neither of the two input parameters nor their interaction effects contributed significantly to the over-cure values in the plane perpendicular to the build direction. Rather, a constant over-curing was seen at all variations of the tested variables ($P < 0.05$). This result suggests that in-plane over-curing is attributable to the absorbance properties of the resin [28]. A transparent resin, like the Pro3dure GR-10, is prone to significant transmission of UV light in the planar directions as each layer of the part is cured. Based on the presented findings, elimination of unwanted over-curing is impractical, and likely impossible, with a resin with such absorption properties. Instead, characterization of over-curing properties at various print settings enables proper compensation in device design for more predictable builds.

Minimum channel cross-sectional area is constrained by the printer and post-processing capabilities: channel cross-sections must be sufficiently large so that they resolve successfully during printing and allow removal of excess resin from within the channels during post-processing. At the selected printing parameters, series of rectangular channels were printed with assorted heights and widths to determine the limits of channel resolution. Results are summarized in Table II. The minimum printed channel cross-sectional area equated to a theoretical value of 0.50 mm^2; it should be noted that the reported channel widths and heights in Table II are the CAD dimensions and not the actual printed dimensions, which are smaller. The narrowest of the channels used in the TAP device had a CAD width of 395 μm, while the width of the corresponding printed channels measured approximately 354 μm, i.e., a reduction of about one pixel, matching the average offset found in the linear fit from the data of the metrology of convex features (see Section II.A).

D. Optical Characterization

Similar to many biomedical microfluidics [42], imaging of the dynamics at the interior of the TAP device is critical, e.g., to verify tumor uploading, to capture fluorescence images

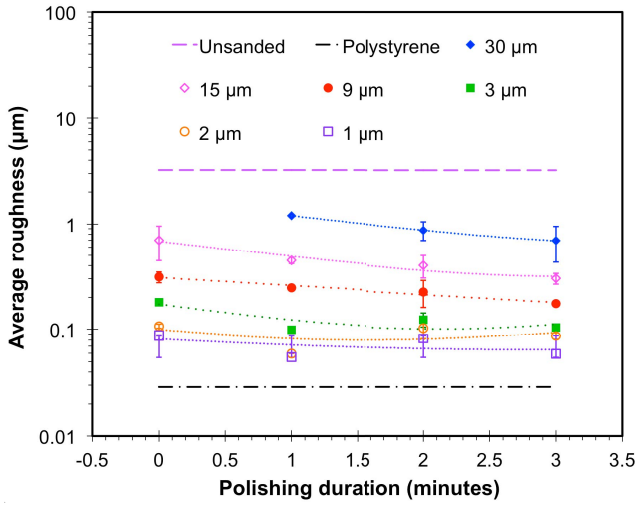

Fig. 3. Arithmetic average surface roughness of Pro3dure GR-10 3DP parts vs. polishing time for six sandpaper grit sizes. Roughness of the untreated surface and of the polystyrene reference surface are also shown.

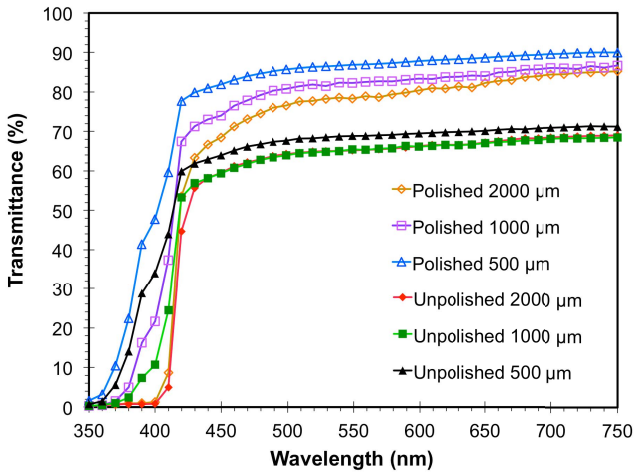

Fig. 4. Transmittance vs. light wavelength for 3DP Pro3dure GR-10 layers of various thicknesses and surface finishes. Unpolished surfaces show little increase in transmission–even with reduction in material thickness.

of intra-channel cell aggregates. An ideal printable material compatible with external optical interrogation must be transparent to visible light (390 nm–700 nm) and have no autofluorescence [43].

The bottom surface of DLP-SLA objects is too rough to permit adequate imaging of the device's interior without additional surface modification; the roughness results from the direct contact of the base of the printed part with the textured surface of the build platform, which ensures adequate adhesion of the object during printing. Multiple surface treatments were explored, including application of a thin layer of clear nitrocellulose coating. Although the coating markedly improved visualization through printed surfaces, the resulting resolution was insufficient for the desired application. Polishing of the device bottom surface produced superior results, enabling the visualization of single cells within the device's channels.

Surface polishing was conducted in six stages and characterized using profilometry. The platform-facing side of unpolished printed parts had an average roughness equal to 3.16 ± 0.095 μm, while the average roughness of a polystyrene culture dish used as target was estimated at 29 ± 21 nm. Printed parts were polished making small-radius circular movements with a constant applied force and rotation frequency for durations equal to 1, 2, or 3 minutes. A Form Talysurf PGI profilometer (Taylor Hobson, Leicester, UK) measured average roughness ($n = 2$) of the polished surfaces at these assigned durations for each of the six grades of 3M Micron Graded Wet/Dry polishing paper: 30 μm, 15 μm, 9 μm, 3 μm, 2 μm, and 1 μm (ZONA, Bethel CT, USA); the results are shown in Fig. 3. The average roughness of the sanded surfaces was reduced to 59 nm $\pm$ 14 nm, i.e., three orders of magnitude smoother and of the same order of magnitude as the surface roughness of the polystyrene target.

The absorbance of printed samples was measured for wavelengths ranging from 350 to 750 nm in 10-nm increments using a SpectraMax M2 plate reader (Molecular Devices, Sunnyvale CA, USA) to verify adequate transparency of the resin Pro3dure GR-10. The absorbance A is defined as

$$A = \log\left(\frac{I_o}{I}\right) \tag{1}$$

where I is the intensity of the light transmitted by the sample and I_o is the original light intensity. Printed chips were sized to fit snugly at the bottom of a Falcon 96-well plate with heights equal to 500 μm, 1000 μm, or 2000 μm. The platform-facing side of half of the disks (i.e., three samples for each height) were polished as previously described. Samples were first cleaned in distilled water and placed into a Falcon 96-well plate with 250 μL of distilled water. Two additional wells, without any printed disks, were filled with 250 μL of water to act as blanks. Absorbance measurements for the blanks were averaged and subtracted from the sample measurements for the respective wavelengths. From these measurements, the absorbance of the printed objects can be estimated. Polished samples exhibited reduced absorbance values for all sample thicknesses. Absorbance readings are high at shorter wavelengths, but reach minimum values at approximately 420 nm (blue light) and remain relatively constant up to 750 nm. Therefore, the resin Pro3dure GR-10 is transparent across most of the visible spectrum, with the exception of the near-UV wavelengths–this is not surprising because the DLP-SLA printer uses an array of 405-nm diodes to expose the printable resin. From the absorbance data, the transmittance T can be calculated given that

$$\mathrm{T} = \left(\frac{\mathrm{I}}{\mathrm{I_o}}\right) = 10^{-\mathrm{A}} \tag{2}$$

The net effect of polishing the surface of the Pro3dure GR-10 3DP objects is a 12% to 19% increase in the transmittance for wavelengths above 500 nm (Fig. 4). The measured transmittance of the polished 500 μm thick samples is above 80% for visible light, plateauing at approximately 90%. Microfluidic devices fabricated from PDMS have been deemed optically acceptable for microscopy when transmission reaches 80% [44],[45]. In the TAP device, images are captured through 300 μm to 500 μm-thick polished, printed walls.

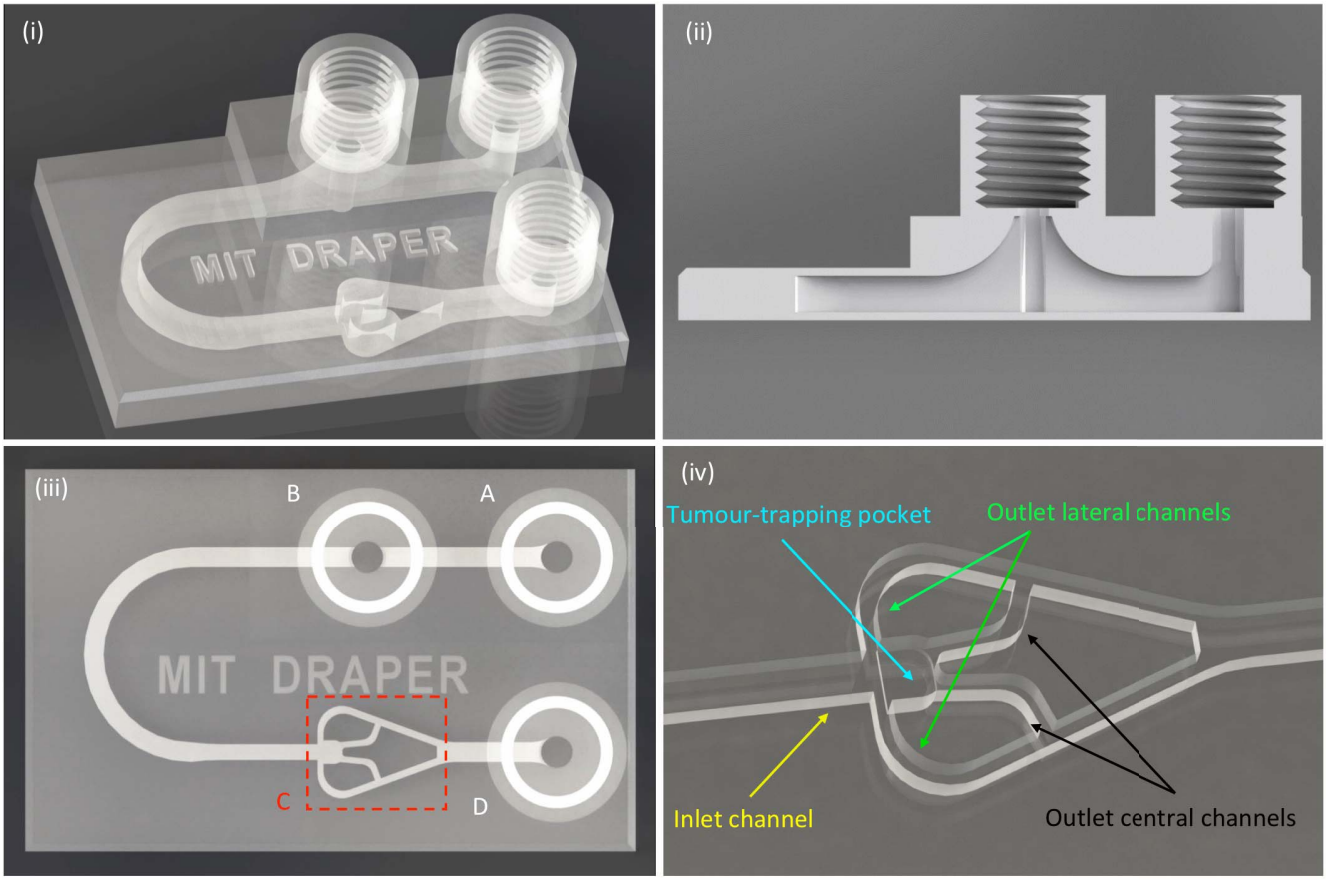

Fig. 5. (i): Translucent 3D schematic of TAP device; (ii): cross-section schematic of TAP device showing the architecture of the bubble trap; (iii): top view schematic of TAP device showing inlet port for media and lymphocytes (A), bubble trapping port for evacuation of trapped air (B), tumor trapping region (C), and device outlet (D); (iv): translucent 3D schematic showing a close-up of the tumor-trapping region with inlet and outlet channels (notice that the tumor-trapping pocket extends below the plane of the channels).

The non-fluorescence characteristics of Pro3dure GR-10 are sufficient for the visualization requirements of the intended application, i.e., resolution of individual cells on the order of 10 μm in size [46] (see Section V.A).

III. Device Design

The TAP device consolidates multiple functional components into a single 14 mm (height) by 24 mm (width) by 38 mm (depth) monolithic chip (Fig. 5). The external in-plane dimensions of the TAP device are governed by the capabilities of the DLP-SLA printer used in this study (a Pico Plus 27 with 24.25 mm by 38.67 mm maximum printable area), while the out-of-plane dimension of the microfluidic chip reflects the separation between the objective and condenser of the confocal microscope Zeiss LSM 880 (Carl Zeiss AG, Oberkochen, Germany) utilized to conduct fluorescence imaging.

The size, distribution, and orientation of certain features of the TAP device reflect functional needs and dimensional constraints. For example, the fluidic ports are oriented vertically (i.e., in the direction of the printed layers) to better resolve the threads, their vertical dimensions (with accompanying fluidic connectors attached) fit within the out-of-plane available distance in the confocal microscope, and the printed fluidic ports have enough threads to reliably interface with specific commercial microfluidic fittings (IDEX Health & Science LLC, Oak Harbor WA, USA).

The internal dimensions of the TAP device (e.g., channel cross-sections) reflect the conclusions of the characterization conducted on the printable material Pro3dure GR-10 (see Section II), the limitations of the printer used (e.g., pixel size), and a particular design architecture implemented to trap a tumor fragment and provide a dynamic microenvironment for perfusing and sustaining such tumor. Although other designs were explored [47], the design reported in this study is the most refined/iterated of those considered.

During operation of the TAP device, incoming media, fluorescent markers, and treated or untreated lymphocytes flow past a bubble evacuation chamber, where unwanted air is removed from the system. The fluid solution is then routed towards a tumor biopsy fragment secured inside a tumor-trapping pocket; multiple flow paths permit media flow through and around the fragment. In future studies with immune cells circulating in the media, lymphocytes can flow within close contact of the tumor sample; if activated by immunotherapy treatments, the immune cells can bind to and kill the cancerous tissue. Threaded connectors at the inlet and outlet ports provide a means to securely attach fluid lines with an airtight seal using commercial microfluidic fittings. During the imaging process, the TAP device with attached fluidic

connectors is positioned between the microscope objective, right below the chip, and a fixed condenser, above the device; imaging is conducted through the bottom of the device.

A. Microfluidic Channel Architecture

Channel specifications are guided by design requirements and constrained by fabrication limitations: on the one hand, the primary (i.e., inlet) channel that transports the tumor to the trap must be sufficiently large to prevent channel clogging by tumor samples; on the other hand, the branched (i.e., outlet) channels downstream of the tumor-trapping region must be small enough so tumor fragments cannot pass through to the device outlet. Ultimately, the minimum channel dimensions are dictated by printer and post-processing capabilities. Channel cross-sections must be sufficiently large to permit successful resolution during printing and removal of uncured resin from within channels during post-processing. Rectangular cross-section channels (heights larger than widths) with filleted corners were utilized in the design to help achieve these objectives. The rounded corners decrease the surface area-to-volume ratio of the channel compared to a rectangular channel with sharp corners, reducing their hydraulic resistance [1] without producing the image distortion that arises in channels with circular cross-section. In addition, the filleted shape mitigates stagnation of fluid and cells in the regions near the corners.

The cross-sectional area of the inlet channel is approximately equal to the summed cross-sectional areas of the outlet channels that directly connect to the pocket; therefore, sudden and large changes in velocity and shear stress are avoided, despite narrowing of outlet channels. However, the additional wall surface area, introduced at the point of channel branching, does lead to increased hydraulic resistance; nonetheless, the wall at the channel branching is essential to trap the tumor fragment.

Outlet channels are sized such that tumor fragments larger than approximately 350 μm in diameter cannot pass through. Four total outlet channels diverge symmetrically from the tumor-trapping region; for clarity, we describe the two sets of mirrored channels as being either *laterally* or *centrally* positioned–where flow in the lateral channels experiences the greatest directional diversion from the primary fluid stream. Two lateral outlet channels branch off of the primary inlet channel immediately upstream of the tumor-trapping pocket. Flow is diverted suddenly and symmetrically; in the process of tumor fragment loading, the momentum direction of the incoming fragment and the un-diverted fluid are unaffected by the equal and opposite siphoning off of flow, and the plug-like tissue is guided to the centrally-located tumor pocket. The two central outlet channels originate downstream of the pocket and produce limited disruption in flow momentum. These channels serve to guide the tumor into place during the loading process, permitting evacuation of fluid in front of the tumor as the tissue enters the tumor-trapping pocket. After loading, the continued flow through the central outlet channels secures the tissue in place; physical restriction by the device geometry coupled with the suction generated through the central channels by the pressure difference between the tumor pocket and the lateral and central outlet channel junctions restricts movement of the tissue sample.

For sample visualization, channel positioning within the device must account for the dependence of light transmission on material thickness. For highest image quality, channel walls through which samples are imaged were constructed as thin as possible without risking structural integrity. In the TAP device, samples are imaged through the bottom surface of the device. As such, the bottom channel walls are positioned 500 μm or less from the base of the chip. Within the tumor-trapping zone (i.e., where image quality is most critical) the floor of the tumor pocket is only 300 μm from the base of the chip.

Avoidance of complete occlusion of a channel by a tumor fragment was achieved by offsetting the tumor pocket so that its base sits 200 μm below the base of the inlet and outlet channels, and by designing rectangular channels with a height larger than the anticipated tumor fragment size. The extended tumor viability test (see Section V.B) suggests that any non-uniformity in the flow does not significantly hinder tumor viability over time. In future studies with the TAP device involving circulating lymphocytes, the non-symmetry of flow in the TAP device may need to be further investigated.

B. Tumor-Trapping Zone

The tumor-trapping zone sits at the intersection of the primary inlet channel and four smaller, diverging outlet channels; when trapped, the tumor resides in a sunken pocket at the aforementioned intersection. The elevation change between the pocket and surrounding channels prevents unwanted regurgitation of tumor tissue. The tumor pocket is constructed large enough for sizable tumor fragments to sit fully within the cavity and small enough that tumor-infiltrating lymphocytes (TILs) flowing past the tumor would likely have their flow path disrupted by the biopsy fragment. The pocket makes the positioning of the tumor fragment straightforward and consistent, facilitating its imaging.

C. Bubble Trap

Bubbles can be inadvertently introduced to the chip during the tumor loading process, or via the incoming flow of media and lymphocytes. Bubbles can adversely impact experimental results and should be prevented from entering the system. Incorporation of a bubble trap into the design allows for easy removal of gas introduced by either mechanism. An in-line bubble trap eliminates the need for an external air removal device, reducing the number of required connections and the risk of unwanted trapping of circulating TILs at these connector sites. Additionally, inclusion of the bubble trap within the device reduces overall fluid volume requirements.

The bubble trap is designed to cause limited disruption of the primary flow path and positioned such that bubbles introduced via the device inlet can be passively removed prior to reaching the tumor site. The vertical cross-section of the bubble trap is a parabolic “chimney” that facilitates removal of bubbles from the flow via gravity. The bubble trap ends in

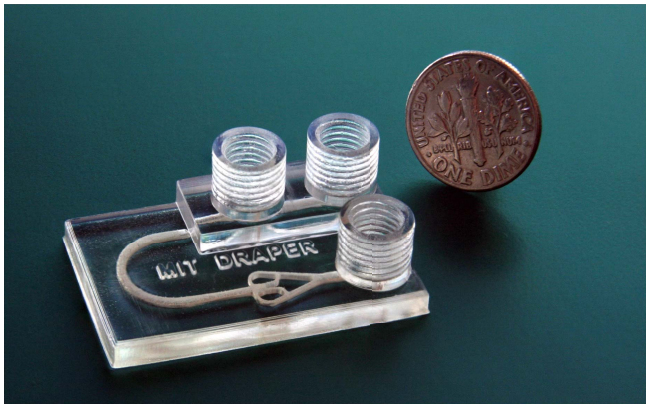

Fig. 6. 3DP TAP device near a US dime for comparison. The tumor-trapping pocket and channels can be seen though the top surface, while the bubble trap is visible as a reflection on a lateral edge of the device.

a threaded port that connects to a syringe, allowing evacuation of gas from the top of the chimney as needed.

D. Tumor Loading

Tumor fragments are introduced into the device with a micropipette via the bubble evacuation port of the bubble trap– this way, any bubbles introduced during the loading process can be readily evacuated. Once the tumor has been placed in the primary channel, the bubble trap is reconnected to the air relief syringe. Initiation of flow through the device inlet drives the tumor through the channel and into the tumor pocket, where the sample remains for the duration of the experiment.

IV. Device Fabrication

The TAP devices were fabricated with an Asiga Pico Plus 27 DLP-SLA printer in Pro3dure GR-10 resin. The printer is contained within a table-top cleanroom environment with HEPA filtering. To print a device, first, CAD models were developed in SolidWorks 2016 (Dassault Systèmes SolidWorks Corporation, Waltham MA, USA) and saved as STL files. Next, using the Asiga Composer software, the CAD models were oriented such that the base of the part was flush with the build platform; print settings were adjusted to a layer thickness of 100 μm and curing offset value of 40 μm. The Composer software generates a file that is transferred to the printer and that can be run untethered. The object is then printed, layer by layer: the entirety of each layer cures simultaneously when a patterned array of pixels directs UV light onto a thin sheet of resin between the build platform and the bottom of a vat of printable feedstock. Between build layers, the platform retracts to allow the bottom of the vat to refill with un-cured resin and to offset its positioning to reflect the addition of the newly generated layer. After printing, the devices were rinsed in isopropyl alcohol (IPA) and dried with a nitrogen gun; the fluidic ports were used to inject IPA to the microchannels, removing any uncured material filling in the internal cavities. Once free of excess resin, the parts were cured in a UV light chamberfor 10 minutes. The bottom surfaces of the cured parts were polished to improve optical transparency of the material.

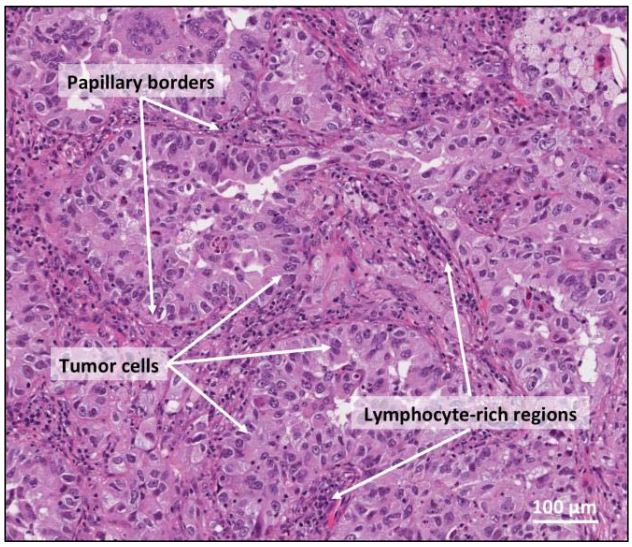

Fig. 7. Haematoxylin and eosin stained histology slice from the tested biopsy sample provided by CHTN. There is a dense concentration of tumor cells within the tumor tissue.

Fig. 6 shows a printed TAP device next to a US dime for comparison.

V. Experimental Results

A. Tumor Trapping

Stained tumor fragments were inserted into the device to ensure consistent capture. Human tumor biopsy samples were obtained from the Cooperative Human Tissue Network (CHTN, Eastern Division, Philadelphia PA, USA). The tissue utilized in these experiments is a non-invasive papillary lung adenocarcinoma originating from a white, 57-year-old female. Histology of the tumor tissue evidences a dense concentration of tumor cells (Fig. 7). The biopsy sample was stabbed with a hollow needle to mechanically extract fragments ranging approximately 400 to 800 μm across. The tumor fragments were incubated at 4 °C for one hour in a solution of CellTracker Green CMFDA Dye (ThermoFisher Scientific, Waltham MA, USA) and PBS at a concentration of 1:500 by volume. The CMFDA dye traverses cellular membranes and is metabolized by live cells into fluorescent and membrane-impermeable by-products. The fluorescent by-products are retained within live cells for upwards of 72 hours [48], enabling prolonged monitoring of cell viability.

After incubation in CMFDA solution, dyed tumor fragments were inserted into the 3DP TAP. Flow from the inlet port guided the tumor fragment through the primary channel to the tumor-trapping zone within the device, eventually landing within the tumor pocket. Fluorescence microscopy confirmed successful tumor fragment trapping (Fig. 8). Given that the CMFDA stain requires cellular uptake and metabolism to generate membrane-impermeable by-products with fluorescent characteristics, and in light of the size and shape of the observed features in Fig. 8, we believe that such objects are individual cells. However, we cannot confirm, and do not assert, that the cells can be identified as are either tumor cells or stromal/vascular cells.

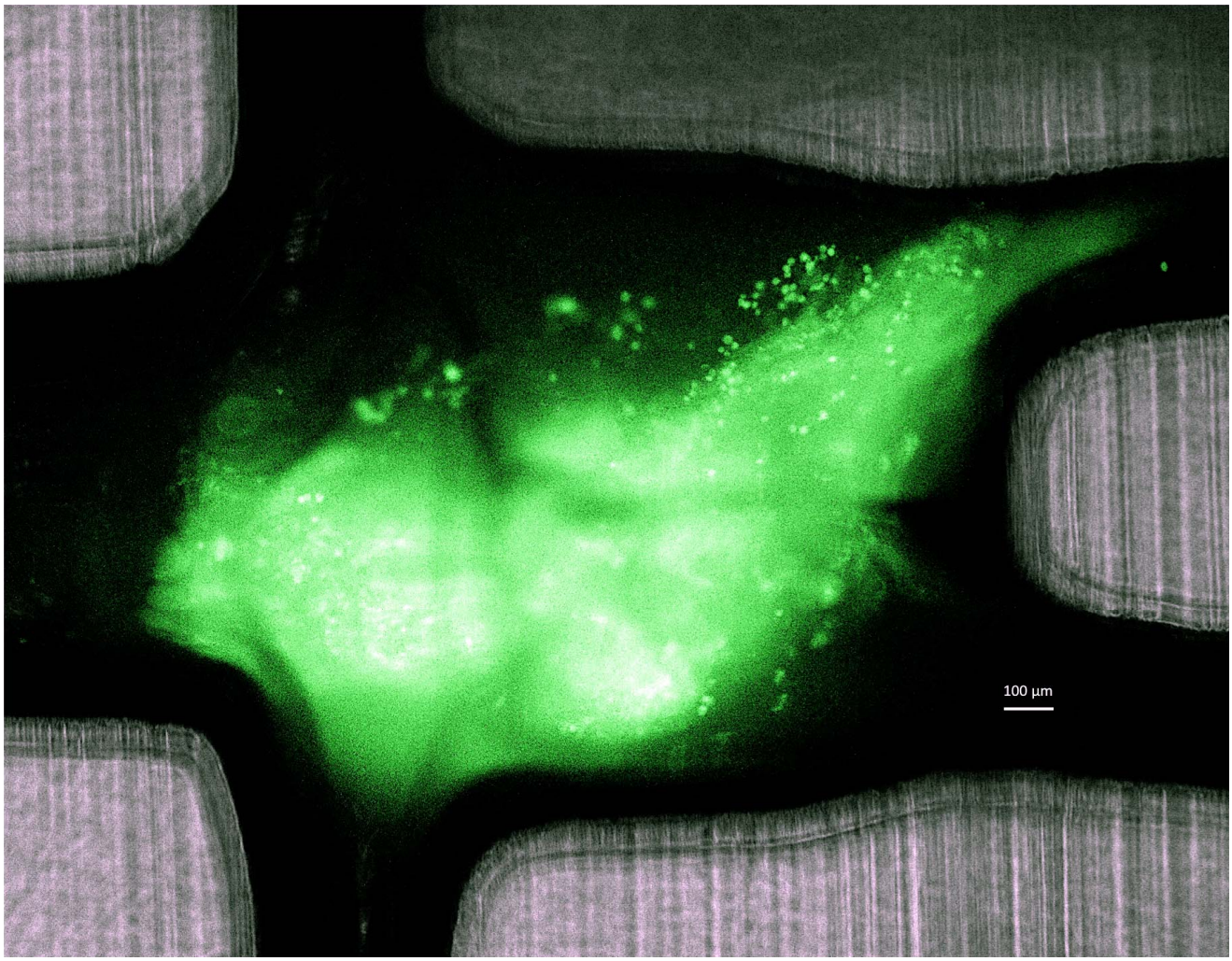

Fig. 8. Overlaid bright-field and fluorescence images of a 3DP TAP device; single cells within a trapped, stained tumor fragment are visible.

B. Extended Tumor Viability

To be useful in the study of chemotherapy or immunotherapy effects on tumor fragments, the TAP must provide an environment which can sustain tumors in the presence of perfusion and the absence of therapeutics. Therefore, a long-term tumor viability experiment was conducted to verify that tumor fragments could be sustained within the printed device for an extended period of time.

1) Tumor Fragmentation and Staining: A human tumor was mechanically divided into fragments roughly 450 μm in size as described before. Studies by Grimes *et al.* indicate that a spheroid radius greater than 233 ± 22 μm exceeded the diffusion distance of oxygen and the tissue exhibited hypoxic effects [49]. Therefore, tumor fragments with a minimum dimension no greater than 450 μm were selected for the long-term tumor viability tests to reduce the risk of cell death resulting from hypoxia. The tumor fragments were stained with CellTracker Green CMFDA Dye for 1.5 hours prior to insertion into the TAP device.

2) System Preparation: System components, including connectors, tubing, and the printed platform, were autoclaved at 121 °C, and final assembly steps were executed in a biosafety cabinet. CMFDA-stained tumors were inserted into devices primed with RPMI with 10% FBS and 1:100 Penicillin/Streptomycin medium containing APC Annexin V (ThermoFisher Scientific, Waltham MA, USA), a fluorescent indicator of apoptosis, at a concentration of 1:2000 (APC/PBS by volume). Media solution also included IgG-1 monoclonal antibodies (Biolegend, San Diego CA, USA) at a concentration of 1:500. The IgG-1 antibody is an isotype control for the anti-PD-1 monoclonal antibody, a form of active immunotherapy which will be evaluated in future work. Media solutions were replenished with freshly mixed replacements at every 24-hour time-point. Flow through the system was maintained by a Standard PHD ULTRATM CP Syringe Pump (Harvard Apparatus, Holliston MA, USA) at a flow rate of 5 μL/min to continuously deliver nutrients to the tumor and remove metabolic products.

3) Selection of Flow Conditions: Maintenance of appropriate shear stress levels experienced by the tested tissue is critical to ensuring tissue viability and physiological relevance of the platform. Computational fluid dynamics guided the selection of an appropriate volumetric flow rate for experi-

mentation. The device CAD geometry, adapted to reflect actual printed dimensions, was imported into ANSYS Fluent R16.2 (ANSYS, Canonsburg PA, USA). The flowing medium was approximated as water and a Runge-Kutta-solved, κ-ε fluid model with standard wall function was employed to analyze the flow. In the simulations, the velocity at the inlet port was set to 1×10^{-4} m/s (i.e., the approximate average velocity at the desired flow rate of 5 μL/min) with a turbulent intensity of 5%, and Turbulent viscosity ratio of 10. A SIMPLE solution scheme with default settings was selected for the solution method. With a volumetric flow rate of 5 μL/min and an oversized tumor diameter of 1mm, estimated shear stresses are over an order of magnitude smaller than the upper bound of physiologically-relevant shear stresses reported by Holton *et al.*, i.e., 0.04 Pa [14].

4) Monitoring Tumor Health: At 24, 48, and 72 hours after tumor insertion into the TAP device, fluorescence images were taken on a series of focal planes with a ZIESS LSM 880 confocal microscope (ZEISS USA, Peabody MA, USA). The series of images, or stacks, spanned the entirety of the tissue depth. At a scanning step size of 1.15μm, the number of images acquired per sample per day ranged from 214 to 405 depending on the shape and orientation of the tumor fragment (Fig. 9). Each set of acquired images was analyzed to determine the area of viable tissue (exhibiting only green, i.e., CMFDA stain), the area of tissue exhibiting indicators of apoptosis (only red, i.e., APC Annexin V stain), and area of dying tissue (which expressed both green and red stains). For each time point, the viable tumor fraction, VTF, was determined by dividing the summed viable area of an imaging stack, $A_{green-only}$, by the total evaluated tumor area of that image series, A_{total}

$$VTF = \frac{\sum A_{green-only}}{A_{total}}. \tag{3}$$

The dead tumor fraction, i.e., *DTF*, and dying tumor fraction, *DyTF*, were similarly obtained using the summed area of dead tissue, $A_{red-only}$, and the summed area of dying tissue, $A_{green-red}$:

$$DTF = \frac{\sum A_{red-only}}{A_{total}}, \tag{4}$$

$$DyTF = \frac{\sum A_{green-red}}{A_{total}}. \tag{5}$$

The resulting fractional tumor compositions of fragments sustained in the TAP device are shown in Fig. 10. The viable fraction of tumor tissue declines slightly over the course of the test from 94.2% after 24 hours in the device, to 91.9% after 72 hours within the device. The result demonstrates that the TAP device can be utilized to sustain live tissue fragments taken directly from an individual for a period of at least 72 hours. Importantly, in future experiments involving the TAP device, the sustained tumor viability within the printed device provides a necessary control to which tumor responses to small molecule drugs and immunotherapies can be compared.

The presented platform is an early investigation into the realization of a high-throughput analysis system; although heterogeneity of native biopsy tissue presents significant advantages in recapitulation of structurally and physiologically relevant models, it also imparts challenges regarding sample-to-sample variation. While pathology of the tissue can help ensure that selected tissue samples are comprised predom-

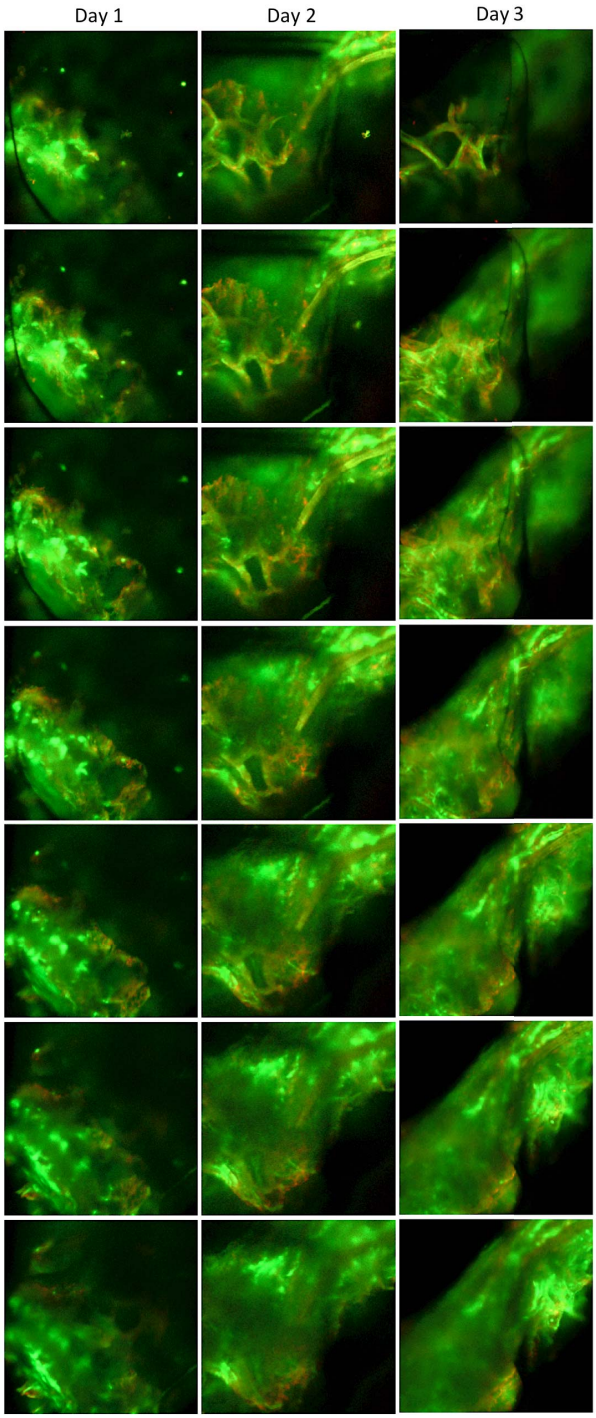

Fig. 9. Selected confocal images of the tumor fragment in the TAP device for days 1 through 3 of the extended tumor viability test. The images are evenly spaced 28.25μm vertically; the images are subsets of the stack of confocal images that were imaged to gather data, which have a vertical step size of 1.15μm. Each column of images corresponds to a different day of test, where the top images are closest to the objective of the confocal microscope and images below are progressively further from the objective. As evidenced by the images, samples exhibited limited change in viability over the 3-day test period.

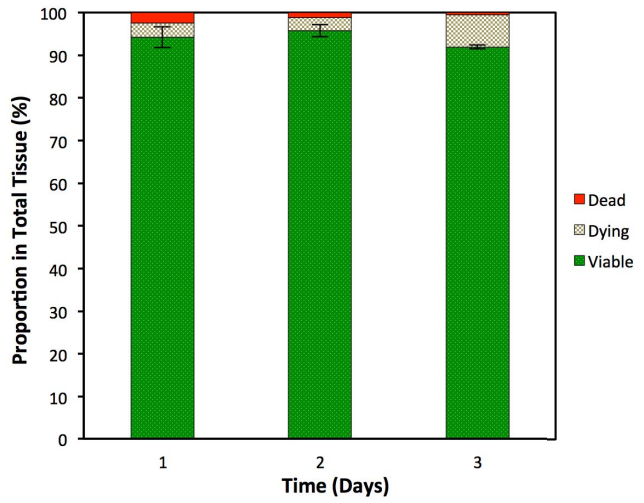

Fig. 10. Fractions of viable tumor (dotted green), dying tumor (checkered brown), and dead tumor (solid red) in a sample sustained within the TAP device over 72 hours of perfusion. Error bars show one standard deviation above and below the average viable tumor fraction for n = 3 samples. Tested fragments originated from two different donor tumors.

inantly of tumor cells, the results of the sample selection process, like the tissue itself, is inherently varied. Consequently, in the application of our technology these factors need to be accounted for —likely by testing a plurality of samples in parallel that minimize the possibility of a false negative. However, even in the case where stromal cells are found within a field of largely tumor cells, the proposed technique provides insight into changes in the tumor cell viability because viable tissue can be consistently sustained over the desired test interval, as shown, and because the drugs to be tested enable immune cells to kill tumor cells and not stromal cells. Substantial changes in viability would therefore be a result of shifts in tumor cell health.

VI. Conclusions and Future Work

We reported the TAP device, i.e., a fully 3DP, monolithic microfluidic that provides a platform for retaining and sustaining tumor tissues *ex vivo* for an extended period under continuous perfusion of media. Overlaid bright-field and fluorescence microscopy images demonstrate trapping of human tumor fragments by the TAP device, and a multi-day trapping experiment demonstrates the ability to sustain a tumor fragment within the device. More broadly, the TAP device is a demonstration of a high-resolution, transparent, biocompatible 3DP microfluidic device with complex geometry that is achievable within the limits of current commercial printing technologies. The presented device can be fabricated and prepared for sterilization and tumor insertion in approximately one hour, which is orders of magnitude faster than the time required for manufacturing and sterilizing a device made with traditional microfabrication methods. The great flexibility of 3D printing permitted the evaluation of over 30 microfluidic design iterations in the span of a few of months.

During device development, we identified the commercial, photopolymerizable resin Pro3dure GR-10 as a material with high resolution, optical transparency, and no cytotoxicity–showing promise as an enabler of monolithic fabrication of complex microfluidic biomedical devices. With the recent availability of 4K UHD DLP chips with ∼5 μm pixel pitch [50] (DLP470TE, Texas Instruments, Dallas TX, USA), we hypothesize that smaller features than those achieved in the resolution matrix experiments could be resolved with Pro3dure GR-10, which should translate in microfluidics with significantly smaller internal features and larger resolution.

We identify several tentative directions for extending the work. First, validation of the TAP device to model the *in vivo* tumor environment to investigate average expected response to pharmaceuticals should be attempted in an application-oriented demonstration. For example, the device could be used for assessing the effect of small-molecule therapies on tumor killing. Small-molecule treatments may attack tumors directly, enabling observation of tumor killing as a function of the dose of a chemotherapeutic agent in this system. Immune checkpoint inhibitors target the immune system, enabling lymphocytes to attack and destroy tumors by blocking pathways hijacked by cancer cells to evade recognition.

Also, the TAP device could be used as a platform for study of interactions between the tumor and circulating immune system for evaluation of patient-specific immunotherapies–efficacy of immunotherapy treatments can vary based upon cancer type and patient biology [36]. The TAP device could enable more judicious administration of chemotherapy and immunotherapy treatments by allowing oncologists to predict patient response rates to particular therapeutic protocols.

Finally, the extent of Pro3dure GR-10's cellular compatibility requires more rigorous evaluation. The availability of high-resolution, transparent, and biocompatible materials that are 3D-printable using relatively inexpensive hardware opens the doors to the creation of geometrically-complex biomedical devices with improved usability and production yields over existing microfluidic technologies. Integration of biocompatible pumps, valves, three-dimensional scaffolds and channel geometries could be achieved in a single microfabrication process [28].

Acknowledgment

The authors would like to thank Nathan Moore and Daniel Doty from Draper for consultations regarding and assistance with biological testing, and Tyler Teague from JETT Research & Proto Products (Fairview TN, USA) for useful conversations on SLA 3-D printing and resins. Tissue samples were provided by the Cooperative Human Tissue Network [51], which is funded by the National Cancer Institute. Other investigators may have received specimens from the same subjects. The New England Independent Review Board (NEIRB) reviewed and approved the human tissue protocol submitted for authorization of this research.

References

[1] D. J. Beebe, G. A. Mensing, and G. M. Walker, "Physics and applications of microfluidics in biology," *Annu. Rev. Biomed. Eng.*, vol. 4, no. 1, pp. 261–286, 2002.

[2] J. M. Ayuso *et al.*, "Development and characterization of a microfluidic model of the tumour microenvironment," *Sci. Rep.*, vol. 6, p. 36086, Oct. 2016.

[3] A. R. Aref *et al.*, "Screening therapeutic EMT blocking agents in a three-dimensional microenvironment," *Integr. Biol.*, vol. 5, no. 2, pp. 381–389, 2013.

[4] W. A. Farahat *et al.*, "Ensemble analysis of angiogenic growth in three-dimensional microfluidic cell cultures," *PLoS ONE*, vol. 7, no. 5, p. e37333, 2012.

[5] S. Parlato *et al.*, "3D microfluidic model for evaluating immunotherapy efficacy by tracking dendritic cell behaviour toward tumor cells," *Sci. Rep.*, vol. 7, p. 1093, Apr. 2017.

[6] Y. Tang, F. Soroush, J. B. Sheffield, B. Wang, B. Prabhakarpandian, and M. F. Kiani, "A biomimetic microfluidic tumor microenvironment platform mimicking the EPR effect for rapid screening of drug delivery systems," *Sci. Rep.*, vol. 7, no. 1, p. 9359, 2017.

[7] X. Y. Wang *et al.*, "An artificial blood vessel implanted three-dimensional microsystem for modeling transvascular migration of tumor cells," *Lab Chip*, vol. 15, no. 4, pp. 1178–1187, 2015.

[8] M. Pisano, V. Triacca, K. A. Barbee, and M. A. Swartz, "An *in vitro* model of the tumor–lymphatic microenvironment with simultaneous transendothelial and luminal flows reveals mechanisms of flow enhanced invasion," *Integr. Biol.*, vol. 7, no. 5, pp. 525–533, 2015.

[9] B. Kwak, A. Ozcelikkale, C. S. Shin, K. Park, and B. Han, "Simulation of complex transport of nanoparticles around a tumor using tumor-microenvironment-on-chip," *J. Control Release*, vol. 194, pp. 157–167, Nov. 2014.

[10] R. Huang, W. Zheng, W. Liu, W. Zhang, Y. Long, and X. Jiang, "Investigation of tumor cell behaviors on a vascular microenvironment-mimicking microfluidic chip," *Sci. Rep.*, vol. 5, p. 17768, Dec. 2015.

[11] K. Shin, B. S. Klosterhoff, and B. Han, "Characterization of cell-type-specific drug transport and resistance of breast cancers using tumor-microenvironment-on-chip," *Mol. Pharmaceutics*, vol. 13, no. 7, pp. 2214–2223, 2016.

[12] R. W. Jenkins *et al.*, "*Ex vivo* profiling of PD-1 blockade using organotypic tumor spheroids," *Cancer Discov.*, vol. 8, no. 2, pp. 196–215, Feb. 2018.

[13] L. J. Y. Ong, A. Islam, R. DasGupta, N. G. Iyer, H. L. Leo, and Y.-C. Toh, "A 3D printed microfluidic perfusion device for multicellular spheroid cultures," *Biofabrication*, vol. 9, no. 4, p. 045005, 2017.

[14] A. B. Holton, F. L. Sinatra, J. Kreahling, A. J. Conway, D. A. Landis, and S. Altiok, "Microfluidic biopsy trapping device for real-time monitoring of tumor microenvironment," *PLoS ONE*, vol. 12, no. 1, p. e0169797, 2017.

[15] M. Madou, "Lithography," in *Fundamentals of Microfabrication: The Science of Miniaturization*, 2nd ed. Boca Raton, FL, USA: CRC Press, 2002, pp. 63–65.

[16] B. J. Van Meer *et al.*, "Small molecule absorption by PDMS in the context of drug response bioassays," *Biochem. Biophys. Res. Commun.*, vol. 482, no. 2, pp. 322–328, 2017.

[17] P. N. Nge, C. I. Rogers, and A. T. Woolley, "Advances in microfluidic materials, functions, integration, and applications," *Chem. Rev.*, vol. 113, no. 4, pp. 2550–2583, 2013.

[18] L. F. Velásquez-García, T. F. Hill, B. A. Wilhite, K. F. Jensen, and C. Livermore, "A MEMS singlet oxygen generator—Part I: Device fabrication demonstration," *J. Microelectromech. Syst.*, vol. 16, no. 6, pp. 1482–1491, 2007.

[19] L. F. Velásquez-García, A. I. Akinwande, and M. Martínez-Sánchez, "A micro-fabricated linear array of electrospray emitters for thruster applications," *J. Microelectromech. Syst.*, vol. 15, no. 5, pp. 1260–1271, Oct. 2006.

[20] B. Gassend, L. F. Velásquez-García, and A. I. Akinwande, "Design and fabrication of DRIE-patterned complex needle-like structures," *J. Microelectromech. Syst.*, vol. 19, no. 3, pp. 589–598, 2010.

[21] R. J. Jackman, S. T. Brittain, and G. M. Whitesides, "Fabrication of three-dimensional microstructures by electrochemically welding structures formed by microcontact printing on planar and curved substrates," *J. Microelectromech. Syst.*, vol. 7, no. 2, pp. 261–266, Jun. 1998.

[22] J.-H. Lee, W.-S. Choi, K.-H. Lee, and J.-B. Yoon, "A simple and effective fabrication method for various 3D microstructures: Backside 3D diffuser lithography," *J. Micromech. Microeng.*, vol. 18, no. 12, p. 125015, 2008.

[23] C. M. Waits, A. Modafe, and R. Ghodssi, "Investigation of gray-scale technology for large area 3D silicon MEMS structures," *J. Micromech. Microeng.*, vol. 13, no. 2, pp. 170–177, 2003.

[24] K. V. Wong and A. Hernandez, "A review of additive manufacturing," *ISRN Mech. Eng.*, vol. 2012, p. 208760, Aug. 2012.

[25] C. M. B. Ho, H. N. Sum, K. H. H. Li, and Y. J. Yoon, "3D printed microfluidics for biological applications," *Lab Chip*, vol. 15, no. 18, pp. 3627–3637, Jul. 2015.

[26] S. Waheed *et al.*, "3D printed microfluidic devices: Enablers and barriers," *Lab Chip*, vol. 16, no. 11, pp. 1993–2013, 2016.

[27] A. K. Au, W. Lee, and A. Folch, "Mail-order microfluidics: Evaluation of stereolithography for the production of microfluidic devices," *Lab Chip*, vol. 14, no. 7, pp. 1294–1301, 2014.

[28] H. Gong, A. T. Woolley, and G. P. Nordin, "High density 3D printed microfluidic valves, pumps, and multiplexers," *Lab Chip*, vol. 16, no. 13, pp. 2450–2458, 2016.

[29] A. P. Taylor and L. F. Velásquez-García, "Miniaturized diaphragm vacuum pump by multi-material additive manufacturing," *J. Microelectromech. Syst.*, vol. 26, no. 6, pp. 1316–1326, 2017.

[30] L. F. Velásquez-García, "SLA 3D printed arrays of miniaturized, internally fed, polymer electrospray emitters," *J. Microelectromech. Syst.*, vol. 24, no. 6, pp. 2117–2127, 2015.

[31] D. Olvera-Trejo and L. F. Velásquez-García, "Additively manufactured MEMS multiplexed coaxial electrospray sources for high-throughput, uniform generation of core–shell microparticles," *Lab Chip*, vol. 16, no. 21, pp. 4121–4132, 2016.

[32] C. I. Rogers, K. Qaderi, A. T. Woolley, and G. P. Nordin, "3D printed microfluidic devices with integrated valves," *Biomicrofluidics*, vol. 9, no. 1, p. 016501, 2015.

[33] *PolyJet Printing Technology*. Accessed: Mar. 1, 2018. [Online]. Available: http://www.stratasys.com/polyjet-technology

[34] Z. Sun and L. F. Velásquez-García, "Monolithic FFF printed, biodegradable, biocompatible, dielectric-conductive microsystems," *J. Microelectromech. Syst.*, vol. 26, no. 6, pp. 1356–1370, 2017.

[35] *Selective Laser Sintering*. Accessed: Mar. 1, 2018. [Online]. Available: https://www.sinterit.com/sinterit-lisa/

[36] N. Restifo, M. Dudley, and S. Rosenberg, "Adoptive immunotherapy for cancer: Harnessing the T cell response," *Immunology*, vol. 12, no. 2, pp. 269–281, 2012.

[37] *Pro3dure GR-10*. Accessed: Mar. 1, 2018. [Online]. Available: http://www.dentona.de/pro3dure-GR-10

[38] E. García-López, D. Olvera-Trejo, and L. F. Velásquez-García, "3D printed multiplexed electrospinning sources for large-scale production of aligned nanofiber mats with small diameter spread," *Nanotechnology*, vol. 28, no. 42, p. 425302, 2017.

[39] F. Zhu, J. Skommer, N. P. Macdonald, T. Friedrich, J. Kaslin, and D. Wlodkowic, "Three-dimensional printed millifluidic devices for zebrafish embryo tests," *Biomicrofluidics*, vol. 9, no. 4, p. 046502, 2015.

[40] E. Schmelzer, P. Over, B. Gridelli, and J. C. Gerlach, "Response of primary human bone marrow mesenchymal stromal cells and dermal keratinocytes to thermal printer materials *in vitro*," *J. Med. Biol. Eng.*, vol. 36, no. 2, pp. 153–167, 2016.

[41] F. Zhu, J. Skommer, T. Friedrich, J. Kaslin, and D. Wlodkowic, "3D printed polymers toxicity profiling: A caution for biodevice applications," *Proc. SPIE*, vol. 9668, p. 96680Z, Dec. 2015.

[42] H. Craighead, "Future lab-on-a-chip technologies for interrogating individual molecules," *Nature*, vol. 442, no. 7101, pp. 387–393, Jul. 2006.

[43] C. Starr, *Biology: Concepts and Applications*. Pacific Grove, CA, USA: Brooks/Cole, 2005.

[44] K.-S. Ma, F. Reza, I. Saaem, and J. Tian, "Versatile surface functionalization of cyclic olefin copolymer (COC) with sputtered SiO_2 thin film for potential BioMEMS applications," *J. Mater. Chem.*, vol. 19, pp. 7914–7920, Sep. 2009.

[45] J. Lee, J. Kim, H. Kim, Y. M. Bae, K.-H. Lee, and H. J. Cho, "Effect of thermal treatment on the chemical resistance of polydimethylsiloxane for microfluidic devices," *J. Micromech. Microeng.*, vol. 23, no. 3, p. 035007, 2013.

[46] D. S. Goodsell, "Introduction," in *The Machinery Life*. New York, NY, USA: Springer-Verlag, 1998, ch. 1, p. 3.

[47] A. L. Beckwith, "Additive manufacturing of microfluidics for evaluation of immunotherapy efficacy," M.S. thesis, Dept. Mech. Eng., Massachusetts Inst. Technol., Cambridge, MA, USA, Jun. 2018.

[48] *CellTracker^{TM} Green CMFDA Dye*. Accessed: Oct. 2, 2018. [Online]. Available: https://www.thermofisher.com/order/catalog/product/C2925

[49] D. R. Grimes, C. Kelly, and M. Partridge, "A method for estimating the oxygen consumption rate in multicellular tumour spheroids," *J. Roy. Soc. Interface*, vol. 11, no. 92, p. 20131124, 2014.

[50] *DLP470TE 0.47 4K UHD DMD Datasheet*. Accessed: May 7, 2018. [Online]. Available: http://www.ti.com/lit/ds/symlink/dlp470te.pdf
[51] *Cooperative Human Tissue Network—Quality Control*. Accessed: Oct. 2, 2018. [Online]. Available: https://www.chtn.org/quality.html

Ashley Beckwith received a B.S. in Mechanical Engineering and a B.S. in Biomedical Engineering from Colorado State University (CSU) in 2015 and her S.M. in Mechanical Engineering from Massachusetts Institute of Technology (MIT) in 2018. She is currently pursuing her PhD in Mechanical Engineering at MIT and is a member of the Velásquez-García Group in the Microsystems Technology Laboratory. Ashley is a Draper Fellow.

Ashley spent five years engaged in biomaterials-oriented research at the Biomaterials Research and Engineering Laboratory at CSU prior to employment as a Quality Engineer focusing on medical device development. Her current research interests include microfluidic technologies, personalized medicine, and implementation of additive manufacturing techniques to better facilitate technology transfer from lab bench to end-application.

Jeffrey T. Borenstein was born in Baton Rouge, Louisiana, and received the B.S., M.S., and Ph.D. degrees in physics from the University at Albany, while simultaneously working at North American Philips Corporation on the development of novel electronic materials for the semiconductor industry. His early work was in semiconductor device physics and MEMS fabrication technologies, and has since moved into BioMEMS and microfluidics with applications in medical devices and drug discovery.

Dr. Borenstein is currently Laboratory Technical Staff and Group Leader, Synthetic Biology and Bio Instrumentation at Draper in Cambridge, Massachusetts. Prior to joining Draper, he was Solar Cell Fabrication Manager at a division of Mobil Oil Corporation. He has 60 issued patents and another 86 patent applications in the fields of MEMS fabrication technology, inertial MEMS sensors, BioMEMS and microfluidics, tissue engineering and drug delivery. Dr. Borenstein has served as Principal Investigator for numerous NIH, DARPA and commercially funded programs in biomedical engineering. He has supervised over 20 graduate students at MIT and currently directs several programs developing new technologies for the pharmaceuticals and medical device industries. His current research interests focus on the development of tools for drug discovery and immuno-oncology, organ assist devices, and implantable drug delivery systems.

He has over 100 peer-reviewed publications in archival journals, and has served as an editor of four books in the fields of semiconductor physics, microfluidics and tissue engineering. Dr. Borenstein is a Standing Member of the ISD Review Panel for the National Institutes of Health, and was inducted in 2015 into the National Academy of Inventors.

Luis Fernando Velásquez-García (M'09–SM'10) received the Mechanical Engineer and Civil Engineer degrees (*magna cum laude* and valedictorian of the School of Engineering in both cases) from the Universidad de Los Andes, Bogotá, Colombia, in 1998 and 1999, respectively, and the M.S. and Ph.D. degrees from the Massachusetts Institute of Technology (MIT), Cambridge, MA, USA, in 2001 and 2004, respectively.

In 2004, after completing his studies, he became a Post-Doctoral Associate with the Microsystems Technology Laboratories (MTL), MIT, where he was appointed as a Research Scientist in 2005. Since 2009, he has been a Principal Scientist and also a Core Member with MTL. He is an expert in micro and nanofabrication technologies. He leads a group that conducts research on micro and nano-enabled multiplexed scaled-down systems that exploit high-electric field phenomena (e.g., electrospray, gas ionization, field emission, X-rays, and plasmas) for space, energy, healthcare, manufacturing, and analytical applications. His current work focuses on additively manufactured micro and nanosystems. He has authored over 44 journal publications and 68 conference proceedings publications, and he is the holder of over 12 issued patents on MEMS/NEMS technologies. He has served as the Co-Chair of the 15th International Conference on Micro and Nanotechnology for Power Generation and Energy Conversion Applications (PowerMEMS 2015).

Dr. Velásquez-García is a full member of Sigma Xi and also a Senior Member of the American Institute of Aeronautics and Astronautics.